Computer Simulations of Pulsatile Blood Flow in Fusiform Models of Abdominal Aortic Aneurysms

P. Vijayajothi[1,2c], M. Kanesan[1] and M. Rafiq Abdul Kadir[2]

[1] *Faculty of Science and Technology, Open University Malaysia, MALAYSIA.*
[2] *Medical Implant Technology Group (MediTeg), Faculty of Biomedical Engineering & Health Science, Universiti Teknologi Malaysia, MALAYSIA.*

Abstract

Flow dynamics have been investigated in model aneurysms under physiologically realistic pulsatile flow condition via computational modeling techniques. The computer simulations are based on finite element method. Vortex pattern emergence and evolution were evaluated. Throughout the bulge in all models regardless of size, the systolic flow was found to be forward-directed. Vortices were initially evident in the bulge during deceleration from peak systole and further expanded during the retrograde flow phase. Flow in larger models become increasingly unstable compared to smaller models. It was also noted that these unstable flow fields were much significant towards the distal half of the bulge models. This increased intensity of turbulent flow fields in larger models may contribute significantly to wall shear stress magnitude and subsequently contributing to higher rupture risks.

Keywords: Computational modelling; flow dynamics; fusiform abdominal aortic aneurysms; pulsatile flow

1.   Introduction

Abdominal aortic aneurysm (AAA) is a dilatation of the infrarenal abdominal aorta that lies between the renal bifurcation and the iliac branches. This pathologic condition has been found to affect 8.8% of the population over the age of 65 and if left untreated it may lead to rupture [1]. The size of the aneurysm and its rate of expansion are parameters widely associated with the risk of rupture [2]. The decision for surgical intervention for patients with AAA is complicated because of the lack of a sufficiently accurate rupture risk index. Based on the results from a number of clinical studies, the maximum/peak transverse diameter (PTD) is widely used [4-7]. In cases where PTD exceeds 5 cm – 6 cm, surgical or endovascular treatment is advised. Although the size of the aneurysm and its rate of expansion are parameters widely associated with the risk of rupture, it is important to understand the flow dynamics of pulsatile flow and its flow implications under an aneurismal condition.

A fundamentally new approach in medical treatment planning and development of predictive methods in clinical applications is computational modelling. Mathematical models can

c Corresponding Author: P. Vijayajothi
Email: vjjothi@yahoo.com   Telephone: +607 2526931   Fax: +607 2541952

help to interpret non-invasive monitoring techniques. The numerical methods used to study AAA development vary from one researcher to another. However, the finite element method is commonly used these days [8-10].

In this paper, we have derived a set of three dimensional finite element equations arising from the mixed velocity-pressure (v-p) finite element method by exploiting the Galerkin method. The fully implicit incremental-iterative numerical procedure was implemented to solve the nonlinear Navier Stokes and continuity equations [11]. This method is then applied to abdominal aortic aneurysm models to study the flow effects.

2. Methods

2.1. Governing equations

The three-dimensional governing equations (momentum and continuity equations) of a viscous incompressible Newtonian fluid (blood) flow, using the indicial notations with the usual summation convention are, respectively;

$$\rho\left(\frac{\partial v_i}{\partial t} + v_j y_{i,j}\right) = -p_{,i} + \mu v_{i,jj} + f_i^B \tag{1}$$

$$v_{i,i} = 0 \tag{2}$$

where v_i is velocity of blood flow in direction x_i, and summation is assumed on the repeated (dummy) indices, i, j = 1, 2, 3. ρ, p, μ, and f_i^B are the fluid density, fluid pressure, dynamic viscosity of fluid and body force, respectively.

2.2. Pulsatile flow

A physiological realistic pulsatile blood flow simulating an *in vivo* cardiac cycle of the abdominal aorta section at rest was imposed at the inlet of the non-dilated aorta entry, as shown in Figure 1 [12]. The mean and peak Reynolds numbers of the pulsatile flow were 525 and 2325, respectively. The pulsatile flow consists of a pulse frequency, ω of 60beats/min, so that the Womersley number $\alpha \approx 12$.

At the inlet of the aorta, the pulsatile flow imposed is considered to be a fully developed flow in an infinitely long straight cylindrical tube model. All velocity components at the fixed vessel wall of the AAA model are prescribed as zero. The no-slip condition at the inner vessel wall was adopted. Along the symmetric plane of the model, the velocity components normal to this plane and the tangential stresses are imposed to be zero. At the outlet of the aorta, the normal and tangential stresses are set to be zero as well respectively (i. e. stress-free condition). Therefore, near the outlet of the aorta the solution differs from the solution in an infinitely long straight cylindrical tube model.

2.3. Aneurysm models

Seven rigid-wall AAA models were computed, each with a different bulge diameter that shows progressively enlargement of AAA. The models had a nondilated inlet tube diameter, d_{AA}=18mm, and a bulge length, L_{AAA}, of $4d_{AA}$. The maximum bulge diameters, d_{AAA}, were distributed from 17.3mm to 44.8mm. As a result, the ratio of bulge diameter to entrance tube diameter of the models, d_{AAA}/d_{AA}, varied from 1.4 to 3.3 as summarized in Table 1 [11]. A typical fusiform AAA geometry is shown in Figure 2.

2.4. Numerical method

The advantage of the mixed velocity-pressure (v-p) formulation is that the pressure, velocity, velocity gradient and stress boundary conditions can be directly incorporated into the

finite element matrix equations. A 21/8 node 3D brick element was used for this three-dimensional analysis. 21 nodes were employed to interpolate the velocities and 8 nodes were employed to interpolate the pressure, hence, providing stable elements expressed by the inf-sup condition of Brezzi-Babuska. The finite element mesh of the model consists of 7,200 elements and 8,450 nodes.
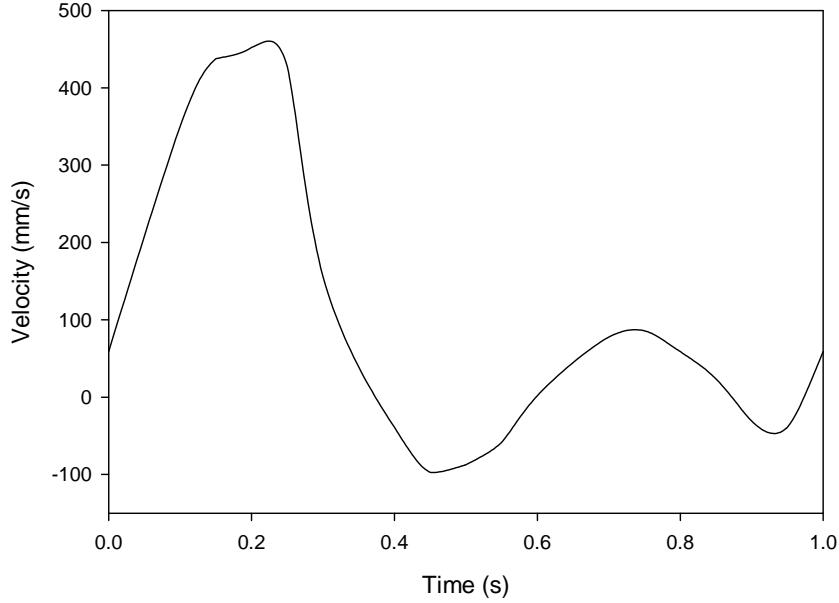

Figure 1. Pulsatile flow cycle

TABLE 1: MODEL ANEURYSM DIMENSIONS

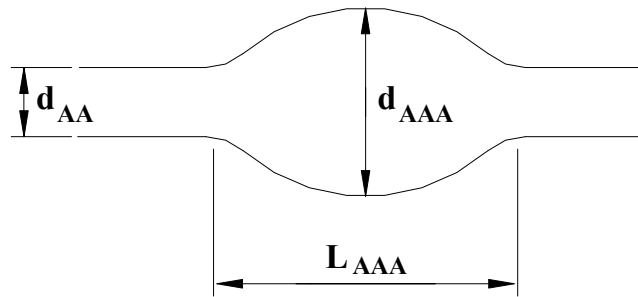| Models	1	2	3	4	5	6	7
d_{AA} (mm)	18	18	18	18	18	18	18
d_{AAA} (mm)	17.3	22.9	30.2	31.5	36.9	39.8	44.8
d_{AAA}/d_{AA}	1.41	1.88	2.27	2.56	2.75	2.97	3.27
L_{AAA}/d_{AA}	4.0	4.0	4.0	4.0	4.0	4.0	4.0

Figure 2. Fusiform AAA geometry

The final incremental-iterative form of the finite element matrix equations for the time-step and the equilibrium iteration "i" is;

$$\begin{bmatrix} \dfrac{1}{\Delta t}\mathbf{M_v} + {}^{t+\Delta t}\mathbf{K}_{vv}^{(m-1)} + {}^{t+\Delta t}\mathbf{K}_{\mu v}^{(m-1)} + {}^{t+\Delta t}\mathbf{J}_{vv}^{(m-1)} & \mathbf{K}_{vp} \\ \mathbf{K}_{vp}^{\mathbf{T}} & \mathbf{0} \end{bmatrix} \begin{Bmatrix} \Delta \mathbf{v}^{(m)} \\ \Delta \mathbf{p}^{(m)} \end{Bmatrix} = \begin{Bmatrix} {}^{t+\Delta t}\mathbf{F}_v^{(m-1)} \\ {}^{t+\Delta t}\mathbf{F}_p^{(m-1)} \end{Bmatrix} \tag{3}$$

where the matrices and vectors are;

$$\left(\mathbf{M_v}\right)_{i\alpha\beta} = \rho\int_V H_\alpha H_\beta dV = \rho\int_V \mathbf{H}^T \mathbf{H} dV \tag{4}$$

$$^{t+\Delta t}\left(\mathbf{K_{vv}}\right)_{i\alpha\beta}^{(m-1)} = \rho\int_V H_\alpha H_\gamma\,^{t+\Delta t}v_{j\gamma}^{(m-1)} H_{\beta,j} dV = \rho\int_V \mathbf{H}^T (\mathbf{H}^{t+\Delta t}\mathbf{v}^{(m-1)})\nabla^T \mathbf{H} dV \tag{5}$$

$$^{t+\Delta t}\left(\mathbf{K_{\mu v}}\right)_{i\alpha\beta}^{(m-1)} = \int_V \mu H_{\alpha,j} H_{\beta,j} dV = \int_V \mu\nabla\mathbf{H}^T\nabla^T \mathbf{H} dV \tag{6}$$

$$^{t+\Delta t}\left(\mathbf{J_{vv}}\right)_{j\alpha\beta}^{(m-1)} = \rho\int_V H_\alpha H_{\gamma,j}\,^{t+\Delta t}v_{i\gamma}^{(m-1)} H_\beta dV = \rho\int_V \mathbf{H}^T (\nabla\mathbf{H}^{t+\Delta t}\mathbf{v}^{(m-1)})\mathbf{H} dV \tag{7}$$

$$\left(\mathbf{K_{vp}}\right)_{i\alpha\delta} = -\int_V H_{\alpha,i} G_\delta dV = -\int_V \nabla\mathbf{H}^T \mathbf{G} dV \tag{8}$$

$$^{t+\Delta t}\mathbf{F_v}^{(m-1)} =\,^{t+\Delta t}\mathbf{R_B} +\,^{t+\Delta t}\mathbf{R_S}^{(m-1)} - \left(^{t+\Delta t}\mathbf{K_{vv}}^{(m-1)} +\,^{t+\Delta t}\mathbf{K_{\mu v}}^{(m-1)}\right)^{t+\Delta t}\mathbf{v}^{(m-1)} - \mathbf{K_{vp}}\,^{t+\Delta t}\mathbf{p}^{(m-1)} \tag{9}$$

$$^{t+\Delta t}\mathbf{F_p}^{(m-1)} = -\mathbf{K_{vp}}^{T\,t+\Delta t}\mathbf{v}^{(m-1)} \tag{10}$$

$$^{t+\Delta t}\left(\mathbf{R_B}\right)_{i\alpha} = \int_V H_\alpha\,^{t+\Delta t}f_i^B dV = \int_V \mathbf{H}^{T\,t+\Delta t}\mathbf{f}^B dV \tag{11}$$

$$^{t+\Delta t}\left(\mathbf{R_S}\right)_{i\alpha}^{(m-1)} = \int_S H_\alpha\left(-^{t+\Delta t}p^{(m-1)}n_i +\,^{t+\Delta t}v^{(m-1)}_{i,j}n_j\right)dS = \int_S \mathbf{H}^T\left(-^{t+\Delta t}p^{(m-1)}\mathbf{n} + \nabla^{t+\Delta t}\mathbf{v}^{(m-1)}\cdot\mathbf{n}\right)dS \tag{12}$$

The left upper index $t+\Delta t$ denotes that the quantities are evaluated at the end of time step. V and S are the volume and the surface of the finite element, respectively. The matrix $\mathbf{H}$ and $\mathbf{G}$ contains the interpolation functions for the velocities and the pressure, respectively. The matrix $\mathbf{M_v}$ is mass matrix, $\mathbf{K_{vv}}$ and $\mathbf{J_{vv}}$ are convective matrices, $\mathbf{K_{\mu v}}$ is viscous matrix, $\mathbf{K_{vp}}$ is pressure matrix and $\mathbf{F_v}$ and $\mathbf{F_p}$ are forcing vectors. $\mathbf{R_B}$ and $\mathbf{R_S}$ are volume and surface forces, respectively.

3.   Results and discussion

As representative examples of the flow field simulations, Figure 3 shows the three-dimensional velocity profiles in Model 1 (d_{AAA}/d_{AA} = 1.88). Six phases of interest within one pulsatile flow cycle were chosen to illustrate the pulsatile velocity fields; t/T=0.035, acceleration to systole; t/T=0.16, peak systolic flow; t/T=0.35, deceleration into retrograde flow; t/T=0.55, peak retrograde flow; t/T=0.77, early diastole; and t/T=0.87, late diastole. In these figures the blood flow direction is referred to the arrow and the various phases of the pulsatile flow are referred to the flow waveform icon within each figure.

Similar flow fields developed in all models at the first two phases of the pulsatile cycle i.e. acceleration to systole (t/T=0.035) and peak systole (t/T=0.16). These flow directed forward throughout the model bulge with velocities being rapid at peak systole compared to during acceleration. In comparison to peak systole, flow deceleration (t/T=0.35) produced reversed velocities at the wall in the proximal half of the model bulge. This indicates the development of a recirculation vortex in this area. This was the first appearance of recirculation or separation in the flow cycle. At this phase, it was confined to the proximal half of the model bulge.

As the flow cycle progressed, the separated region of recirculation along the wall at first increased in length, then was swept away by the developing retrograde flow. At peak reversed flow (t/T=0.55), the flow entered the model from its distal end and exited proximally. Then in early diastole (t/T=0.77) the complicated velocity pattern developed. With little net flow, velocity magnitudes in the proximal half of the bulge decayed to nearly zero, producing nearly quiescent conditions in the proximal half. However, in the distal half of the bulge, the momentum of the fluid was not fully decayed and a core region of flow continued travelling forward. An outer region in retrograde motion surrounded the core, and itself was surrounded by an even thinner outermost layer along the wall travelling forward. This complex pattern indicates the presence of a double

recirculation vortex in the middle and distal half of the bulge. Finally, the distal recirculation vortex dissipated during late diastole (t/T=0.87) and a weak forward flow developed throughout the model.
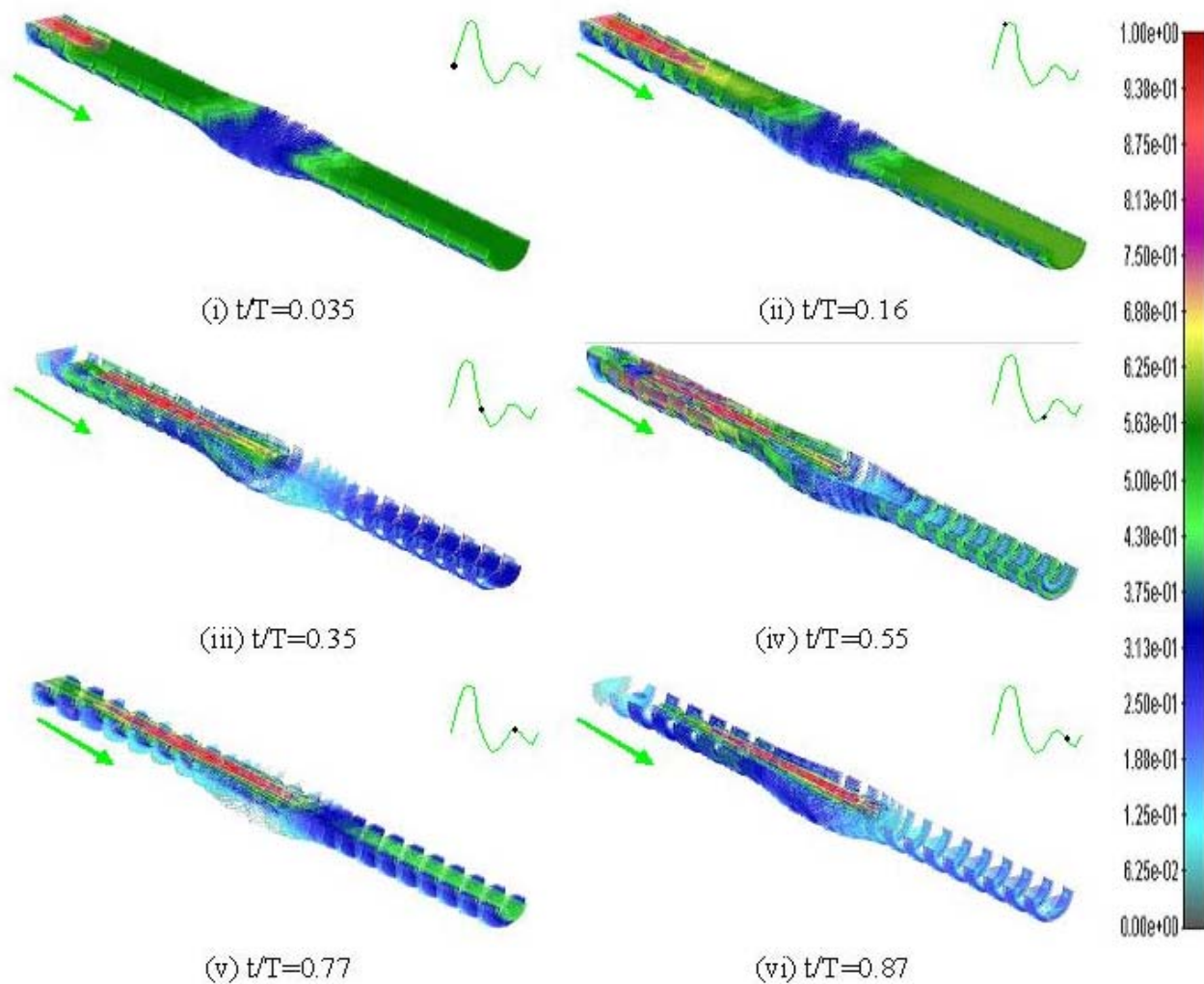

Figure 3. Velocity profiles in model 1 at six phases of the flow cycle: (i) t/T=0.035, acceleration to systole; (ii) t/T=0.16, peak systolic flow; (iii) t/T=0.35, deceleration into retrograde flow; (iv) t/T=0.55, peak retrograde flow; (v) t/T=0.77, early diastole; and (vi) t/T=0.87, late diastole

As comparison between each model, the greatest velocity in the smallest model was approximately 20% larger than in the largest model. In addition during peak retrograde flow, in the smallest models the flow fields was fully directed in the retrograde direction. In the largest models, there remained a core region of forward directed fluid. The other principle difference between flow in the smallest models and that in the largest was that the smallest models lacked a diastolic double vortex with only a single vortex appearing in the distal bulge during diastole. Both the primary vortex and the diastolic double vortex were weakest in the smallest bulges. Figure 4 shows the evolution of vortex intensity at peak retrograde (t/T=0.55) in each model.

The streamlines in Figure 5 illustrate the appearance and evolution of vortices in the flow for peak systole t/T=0.16, flow deceleration t/T=0.35, peak retrograde flow t/T=0.55, and early diastole t/T=0.77 in Model 5. It was observed that for flow acceleration and during early and peak systole there are no vortices but the vortex did form by late systole at the proximal end and during maximum retrograde flow. Also the vortex moves toward to the distal end of AAA during early diastole.
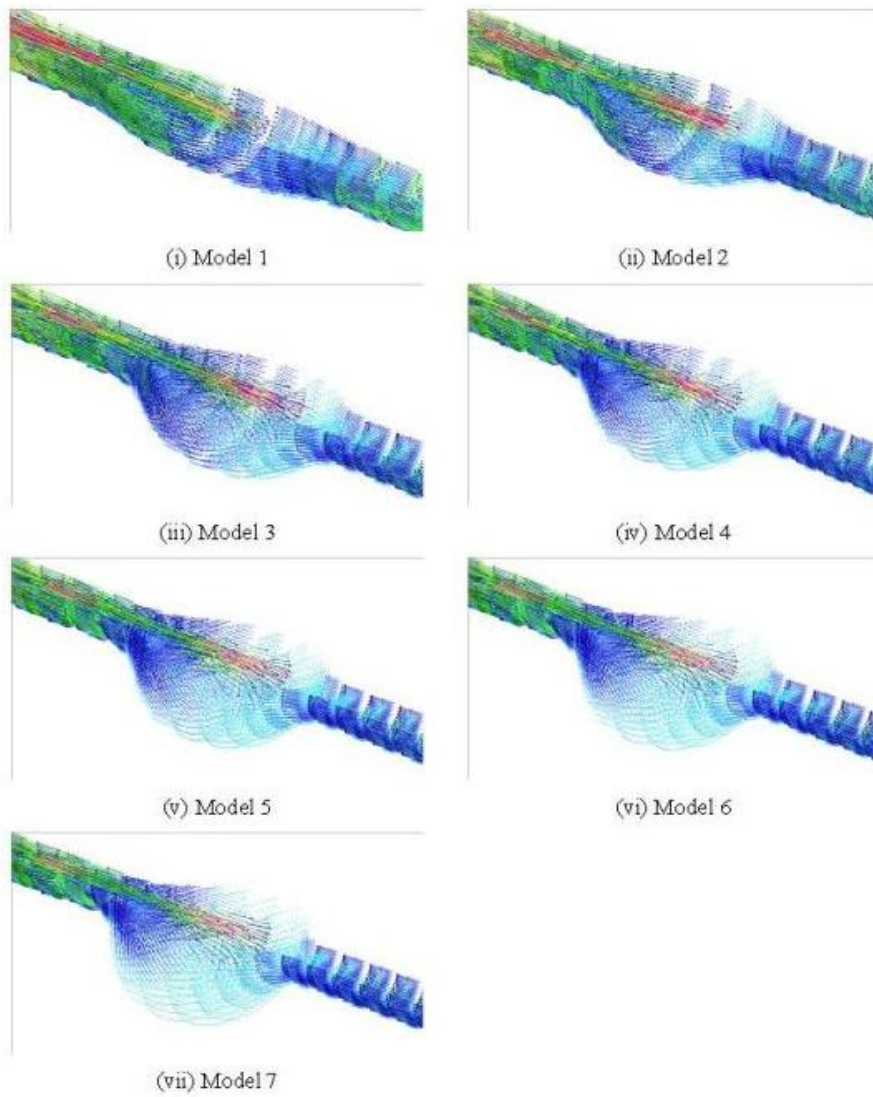
(i) Model 1

(ii) Model 2

(iii) Model 3

(iv) Model 4

(v) Model 5

(vi) Model 6

(vii) Model 7

Figure 4. Vortex evolutions at peak retrograde in all models
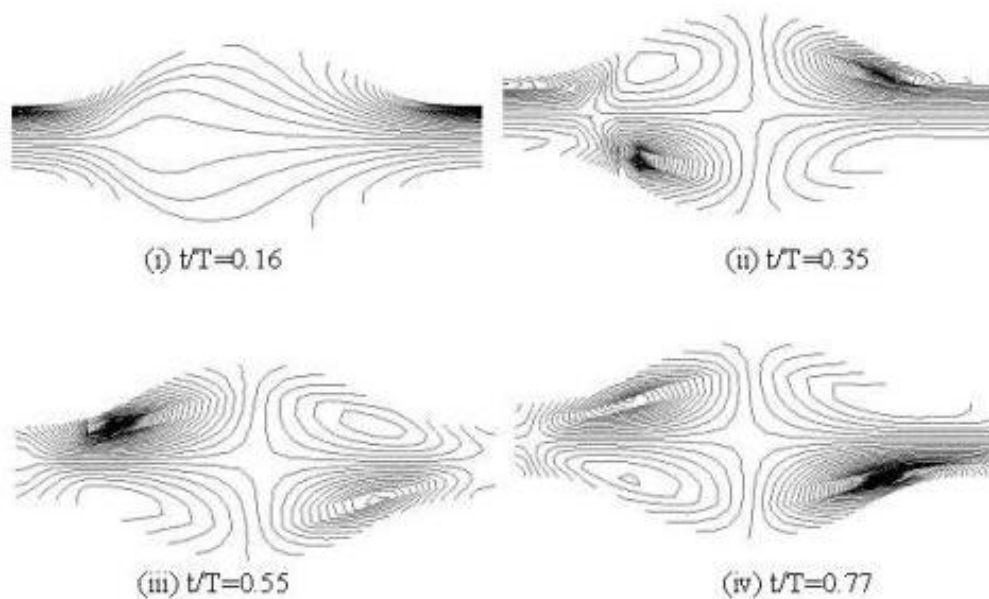

(i) t/T=0.16

(ii) t/T=0.35

(iii) t/T=0.55

(iv) t/T=0.77

Figure 5. Streamlines for the symetry plane of AAA for d_{AAA}/d_{AA} =2.75 for different phases: t/T=0.16 systole, flow deceleration t/T=0.35, peak retrograde flow t/T=0.55, diastole t/T=0.77

Acknowledgement

References

[1]   Cotran RS, Kumar V, Robbins SL. Robbins Pathologic Basis of Decease. London: Saunders 1994.

[2]   Newman AB, Arnold AM, Burke GL, O'Leary DH, Manolio TA. Cardiovascular disease and mortality in older adults with small abdominal aortic aneurysms detected by ultrasonography: the cardiovascular health stud*y*. Annals of Internal Medicine 2001; 134: 182-190.

[3]   Clement Kleinstreuer, Zhonghua Li. Analysis and computer program for rupture-risk prediction of abdominal aortic aneurysm. BioMedical Engineering OnLine 2006; 5:19.

[4]   Myers K, Devine T, Barras C, Self G. Endoluminal Versus Open Repair for Abdominal Aortic Aneurysms. 2001; http://www.fac.org.ar/scvc/llave/intervine/myers/myersi.html.

[5]   Limet R, Sakalihassan N, Albert A. Determination of the expansion rate and incidence of rupture of abdominal aortic aneurysms. Journal of Vascular Surgery 1991; 14: 540-548.

[6]   Fillinger MF, Raghavan ML, Marra P, Cronenwett L, Kennedy E. In vivo analysis of mechanical wall stress and abdominal aortic aneurysm rupture risk. Journal of Vascular Surgery 2002; 36: 589-596.

[7]   Fillinger MF, Marra PS, Raghavan ML, Kennedy EF. Prediction of rupture in abdominal aortic aneurysm during observation: wall stress vs diameter. Journal of Vascular Surgery 2003; 37: 724-732.

[8]   Taylor C & Draney M. Experimental and computational methods in cardiovascular fluid mechanics Annu. Rev. Fluid Mech. 2004; 36: 197-231.

[9]   Quarteroni A, Tuveri M, Veneziani A. Computational vascular fluid dynamics : problems, models and methods. Comp. Visual Sci. 2000; 2: 163-197.

[10] Filipovic N. Numerical analysis of coupled problems: Fluid flow through porous deformable medium with implementation in biomechanics and geomechanics. Ph. D. Thesis, University of Kragujevac, Serbia-Yugoslavia, 1996.

[11] Vijayajothi P, Filipovic N, Kanesan M, Mohamad Rafiq AK. Finite element computation for solving pulsatile blood flow: Relevance in assessing the flow dynamics in abdominal aortic aneurysm. CFDLetter 2010; 2(4): 149-162.

[12] Peattie RA, Riehle TJ, Bluth EI. Pulsatile flow in fusiform models of abdominal aortic aneurysms: flow fields, velocity patterns and flow-induced wall stresses. Journal of Biomechanical Engineering 2004; 126: 438-446.